Origin of quasilocal plasmons in Nb-substituted $EuTiO_3$

A. Chaudhuri,[1,2,*] A. Midya,[3] K. Rubi,[3] X. Chi,[2,3] T. C. Asmara,[1,2] X. J. Yu,[2] R. Mahendiran,[1,3,†] and A. Rusydi[1,2,3,4,‡]

[1]*NUSSNI-NanoCore, National University of Singapore, Singapore 117576, Singapore*

[2]*Singapore Synchrotron Light Source, National University of Singapore, 5 Research Link, Singapore 117603, Singapore*

[3]*Department of Physics, National University of Singapore, Singapore 117542, Singapore*

[4]*National University of Singapore Graduate School for Integrative Sciences and Engineering (NGS), 28 Medical Drive, Singapore 117456, Singapore*

(Received 31 January 2019; revised manuscript received 14 June 2019; published 29 August 2019)

Doped perovskite oxides are promising "material building blocks" for achieving tunable and intrinsically low-loss plasmonic features in the visible- to near-infrared range, which are unlikely to obtain from conventional plasmonic materials. Here, using a combination of spectroscopic ellipsometry, soft x-ray absorption, x-ray photoemission, and ultraviolet photoemission spectroscopic measurements we observe an unconventional tunable low-loss quasilocal plasmon in the IR energy (<1 eV) range in the Nb-substituted perovskite oxide $EuTiO_3$ ($EuTi_{1-x}Nb_xO_3$). This low-loss plasmon oscillation is formed by many-body interactions, an interplay of quasifree d^1 electrons and hybridizations of Eu 4*f*-Ti 3*d* and O 2*p*-Ti 3*d*. We find that the Nb substitution at Ti site modifies the TiO_6 octahedral tilting and, consequently, alters the electronic structure. Our study reveals the importance of charge, orbital, and lattice to generate plasmons in $EuTi_{1-x}Nb_xO_3$.

DOI: 10.1103/PhysRevB.100.085145

I. INTRODUCTION

Plasmons in the infrared energy range are attractive in diverse fields of applications, such as transformation optics [1], photodetection, nonlinear frequency generation [2], biomolecule sensors [3], pharmacology, and many more [4]. However, conventional plasmonic materials have an inherited limitation in the infrared energy range because of their metallic components that usually introduce large negative permittivity and high absorption resulting in high loss in this region [5]. Therefore, the search for a new class of "designer plasmonic materials" in the mid- to near-infrared (IR) range has been the research focus in recent years.

In principle, one could achieve plasmons in IR energy by diluting the free electrons of the metal to redshift the plasma frequency into lower energy range, or by doping a semiconductor to blueshift the plasmon energy towards the desired energy range. While the limiting factor for conventional metals is the high absorption yielding high plasmonic-loss, the fundamental constraint for conventional doped semiconductors is the finite carrier density. Therefore, strongly correlated electron systems such as transparent perovskite oxides are promising, particularly for their ability to tune the optical band gap and charge carrier as well as to confine the electromagnetic radiation in the subwavelength range. However, the plasmonic properties have been so far studied only for a limited number of perovskite oxides, leaving a vast pool of materials largely untapped [1–3].

Therefore, to search for low-energy plasmonic oscillations with low absorption, efforts were made to explore the transparent perovskite oxides for their ability to tune the optical band gap and the charge carrier, as well as to confine the electromagnetic radiation in the subwavelength range. These studies led to discovery of unconventional plasmonic oscillations, which were characterized as non-Drude in nature [6–8]. By tapping the strongly-correlated electronic structures, unconventional plasmons have been reported in thin films of $Sr_{(1-x)}Nb_{(1-y)}O_{3+\delta}$ perovskites family [7].

Recently, a formation of quasilocal electrons was found in bulk perovskites of Nb-substituted $Eu_{0.3}Ba_{0.7}TiO_3$ (hereafter EBTO) [8], which has shown low-loss plasmonic oscillations in the IR-energy range. In Nb-substituted EBTO, it has been revealed that, due to the weak Eu-O hybridizations and the associated screening effect, a systematic increase of partly delocalized electrons is manifested in the form of a Nb-substitution-controlled quasilocal plasmon in the infrared-energy range. The associated electronic band modulation, which is impacted by the onsite screening effect, is responsible also for the insulator-metal transitions (IMT) in the EBTO-10Nb. This study opens up several interesting prospects of band modulation and associated dielectric properties in strongly correlated systems taking the Nb-substituted EBTOs as case-study. Several important questions related to electronic structure and impact of *A*-site cation substitution for the structure in such a perovskite system remain open.

All of these motivate us to study the effect of Nb substitution on the dielectric properties of the prototypical perovskite ETO using a combination of spectroscopic ellipsometry, soft x-ray absorption spectroscopy at Ti $L_{3,2}$ and O *K* edges, x-ray photoemission, and ultraviolet photoemission spectroscopies measurements. We intentionally choose ETO as the parent compound, particularly to reveal the role of the *f* orbital of Eu and its hybridizations. The formation of non-Drude-type

*Corresponding author: nniac@nus.edu.sg
†Corresponding author: phyrm@nus.edu.sg
‡Corresponding author: phyandri@nus.edu.sg

plasmons is observed in 10% Nb-substituted ETO. Notably, the plasmonic energy and the intensity of the loss function are significantly lower than those observed in the 10% Nb-substituted EBTO. Interestingly, the Nb substitution at the *B* site in ETO significantly modifies the octahedral tilting that alters the *f*-*d* hybridizations and forms the quasilocal plasmon. By Nb substitution, the intrinsic insulator ETO becomes a Mott insulator in which the Mott gap narrows with the amount of Nb substitution. However, unlike the Nb-substituted EBTO, in which midgap states were the key for the IMT, there is no IMT observed for ETO up to 10% Nb substitution. Our study strongly suggests the possibility of doping-controlled tunable low-loss quasilocal plasmonic oscillation in the mid-IR energy range (<0.4 eV) in Nb-substituted ETO.

II. EXPERIMENTAL

A. Materials preparations and structural characterizations

$EuTi_{1-x}Nb_xO_3$ ($x = 0.00$, 0.06, and 0.10) polycrystalline samples were synthesized using conventional solid-state reaction method. The stoichiometric amount of Eu_2O_3, TiO_2, and Nb_2O_5 powders was mixed, ground, and annealed at 1200 °C for 24 h in reduced atmosphere (95% Ar and 5% H_2) for reducing Eu^{3+} into Eu^{2+}. After two consecutive grindings and annealings, the powder was pressed into a pellet and then sintered at 1300 °C for 24 h in the same atmosphere. A Philips X'PERT MPD powder x-ray diffractometer was employed for structure characterization at room temperature using Cu Kα radiation. All samples are in single phase and crystallize in cubic perovskite structure with space group *Pm*-3*m* and lattice constant $a = 3.9045$ Å, $b = 3.9087$ Å, and $c = 3.9126$ Å for $x = 0.00$, 0.06, and 0.10.

B. Spectroscopic ellipsometry

In the spectroscopic ellipsometry technique, one measures the relative change in amplitude and phase of a linearly polarized monochromatic incident light upon oblique reflection from the sample. The experimental parameters, the angles Ψ and Δ, defined as $\tan\psi . \exp(i\Delta) = \frac{r_p}{r_s}$ (where r_p and r_s are the complex reflectance coefficients of the polarized light parallel and perpendicular to the plane of incidence, respectively) are measured to extract the dielectric properties of the samples. The spectroscopic ellipsometric spectra (in terms of ψ and Δ) are measured at room temperature and *ex situ* on ETO and Nb-substituted ETOs at three angles of incidence (65°, 70°, and 75°) from the sample normal in the spectral range of 0.4 to 6.0 eV with a variable-angle spectroscopic ellipsometer (J.A. Woollam Co. VASE). Details of the instrument and the measurement geometry are described elsewhere [9]. The complex dielectric functions ε_1 and ε_2 are extracted by the standard numerical regression procedure, considering an optical model of thick bulk substrate with surface roughness [10]. The model is parametrized with five tri-semioscillators to define the precise optical transitions for the bulk and Nb-substituted ETO samples. WOOLLAM COMPLETE EASE software is used for the entire analysis.

C. X-ray absorption spectroscopy, x-ray photoelectron spectroscopy, and ultraviolet photoelectron spectroscopy

The soft x-ray absorption spectra (XAS) are collected for these samples at the Soft X-ray and ultraviolet (SUV) beamline [11] and Surface, Interface and Nanostructure Science beamline [12] of the Singapore Synchrotron Light Source (SSLS), National University of Singapore. The base pressure in the UHV chamber is maintained at $\sim 2 \times 10^{-10}$ mbar throughout the measurements. The collected Ti L_3 and O-*K* XAS spectra are normalized by the incident photon flux (I0).

The XPS spectra are recorded using an electron spectroscopy for chemical analysis (ESCA) on an Omicron EA125 U7 hemispherical electron spectrometer with monochromatized Mg Kα radiation ($h\nu = 1253$ eV). The spectra are calibrated against the Au $4f_{7/2}$ signal from a Au foil (84.0 eV)

The valence-band structures are measured using ultraviolet photoemission spectroscopy (UPS) radiation generated by a He-gas discharge lamp (He Iα at 21.22 eV), equipped in the same ESCA chamber using the Omicron EA125 U7 hemispherical electron spectrometer. The energy of the UPS spectrum is calibrated by setting the Fermi edge of clean silver at 0 eV. The base pressure is maintained below 10^{-9} mbar during measurements. All spectra were collected at room temperature. No significant charging effects were observed during spectral measurements.

III. RESULTS AND DISCUSSION

A. Dielectric properties and the plasmonic excitation

Experimental Ψ and Δ for ETO, ETO-6Nb, and ETO-10Nb, obtained from spectroscopic ellipsometry measurements, are shown in Fig. 1 together with the fittings. The real and imaginary parts of the complex dielectric function (ε_1 and ε_2) are derived from the measured values of Ψ and Δ, using WOOLLAM COMPLETE EASE software. We calculate the loss function ($-\mathrm{Im}[\varepsilon^{-1}(\omega)]$) of the plasmonic oscillation using the following equation:

$$-\mathrm{Im}\,[\varepsilon^{-1}(\omega)] = \varepsilon_2(\omega)\big/\big[\varepsilon_1^2(\omega) + \varepsilon_2^2(\omega)\big], \tag{1}$$

ω being the angular frequency of the incident photon. We determine normal incident reflectivity R defined as

$$R(\omega) = \frac{[n(\omega) - 1]^2 + \kappa^2(\omega)}{[n(\omega) + 1]^2 + \kappa^2(\omega)}, \tag{2}$$

where n (refractive index) and κ (extinction coefficient) are given by the following equations:

$$n(\omega) = \sqrt{\frac{1}{2}\Big[\sqrt{\varepsilon_1^2(\omega) + \varepsilon_2^2(\omega)} + \varepsilon_1(\omega)\Big]}, \tag{3}$$

$$\kappa(\omega) = \sqrt{\frac{1}{2}\Big[\sqrt{\varepsilon_1^2(\omega) + \varepsilon_2^2(\omega)} - \varepsilon_1(\omega)\Big]}. \tag{4}$$

We show the loss function [Fig. 2(a)] and reflectivity R [Fig. 2(b)], the real part ε_1 [Fig. 2(c)], and imaginary part ε_2 [Fig. 2(d)] of the complex dielectric functions to substantiate the formation of the aforementioned quasifree plasmonic excitations in ETO-6Nb and ETO-10Nb.

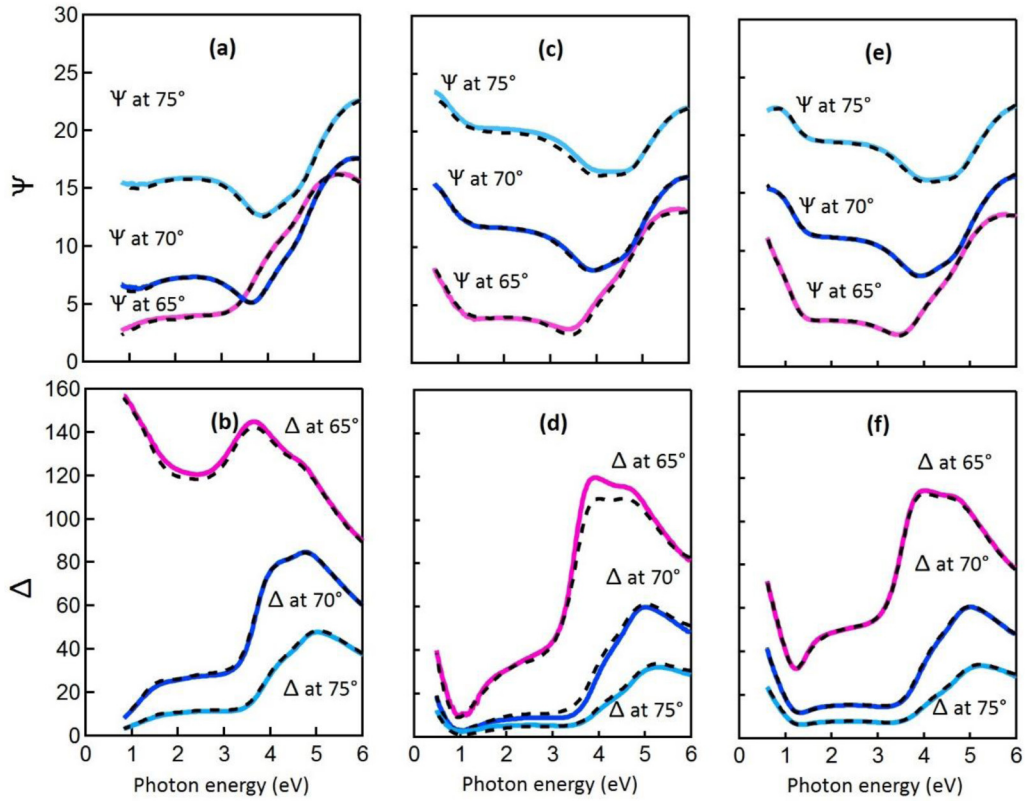

FIG. 1. Experimental (solid curves) and fitted (dotted curves) data of Ψ and Δ for ETO (a), (b), ETO-6Nb (c), (d), and ETO-10Nb (e), (f) obtained at 65°, 70°, and 75°.

In the low-energy range (<1 eV), the loss function of Nb-substituted ETOs shows distinct peaks (for example, the peak at 0.54 eV for the ETO-10Nb) [Fig. 2(a)]. The existence of associated reflectivity edges below 1 eV [Fig. 2(b)] clearly confirms the plasmonic excitation in Nb-substituted ETOs in this IR-energy region. Interestingly, these plasmons are different from the conventional (bulk) plasmon in the sense that the associated ε_1 profiles [Fig. 2(c)] do not go through the *zero crossing*: a fingerprint of Drude oscillation for the free electrons. The nonzero minima in ε_1 corresponding with the plasmonic oscillation indicate the electrons participating in this type of plasmon formation are not free*like* in conventional metal, instead they are quasifree. We also notice that the energy of this type of plasmonic oscillation shows blueshifts within the IR-energy range with Nb substitution. We report the plasmon formation in Nb-substituted ETOs in which the energy of the plasmon oscillation can be controlled within the IR-energy range by the amount of Nb substitution in ETOs. Origin and the mechanism of formation of these quasifree plasmons are elaborated by analyzing further with spectroscopic techniques, namely XAS and UPS.

Among the other transitions observed in Fig. 2(d), the strongest one is at around 5 eV in all three samples. This transition is the fingerprint of the charge transfer (CT) from O $2p$ to the d band [13,14]. There are two critical points/transitions observed below the CT (energy range <3.5 eV) and above the plasmonic range (>1 eV). Similar to the reported profiles of ε_2 by Lee *et al.*, these transitions are at 1.8 and 2.8 eV, which can originate due to the interactions between d and f electrons [15].

B. Local electronic structures of TiO_6 octahedron, XAS at Ti $L_{3,2}$ edge

To understand the effects of Nb substitution on the electronic structures of ETOs, we consider first the XAS of Ti L edge, since the local electronic structure of Ti cation critically controls the (ferro) electric and (ferro) magnetic properties of ETOs [16–20] by virtue of the tilting or the rotation of the TiO_6 octahedra, which alters the spin-lattice coupling and the hybridization between Eu $4f$ and Ti $3d$ and O $2p$.

Figure 3 shows the Ti $L_{3,2}$ XAS spectra obtained from the ETO and Nb-substituted ETOs. The spectra can be classified into well-defined L_3 and L_2 regions with a separation of ∼5.5 eV, taking the spin-orbit coupling into account. Due to the crystal-field interactions, the L_3 and L_2 edges are further split into t_{2g} and e_g subbands. However, the peaks at the L_2 edge are broadened and the detailed features of the peaks are often smeared out due to the Coster-Kronig Auger decay process [21] leaving the L_3 edge for analyzing the XAS spectra. Here, the spectra, shown in the figure, are normalized with respect to L_2 e_g.

A close comparison between the Ti $L_{3,2}$ edge XAS spectrum, collected from the parent ETO compound and Ti^{4+} ion [22], reveals that the Ti ions mostly exist in Ti^{4+} (d^0) states. The gradual increase of the onset of the L_3 e_g edge (∼459 eV)

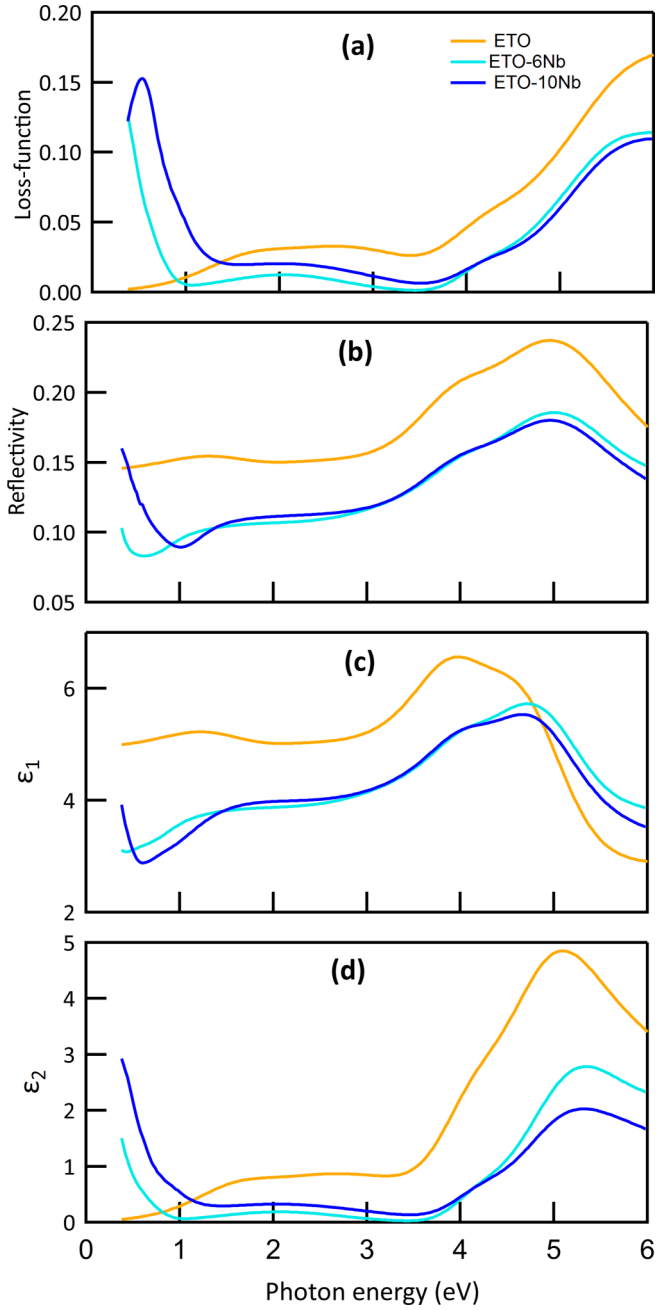

FIG. 2. Comparison of dielectric properties. (a) Loss function. (b) Reflectivity R. (c) Real part (ε_1) of dielectric function. (d) Imaginary part (ε_2) of dielectric function. Color code: ETO (saffron), ETO-6Nb (light blue), and ETO-10Nb (dark blue).

with the Nb substitution and simultaneous decrease of intensity of the t_{2g} peak, imply the formation of Ti^{3+} (d^1) in the ETO-6Nb and ETO-10 Nb: the d^1 electrons have been incorporated into the t_{2g} states.

It is worth noting that the energy positions of the L_3 t_{2g} peaks remain almost unaltered with Nb substitution while the L_3 e_g peaks gradually convert from an asymmetrical (in ETO) to a more symmetrical shape (Nb-substituted ETOs) and move slightly towards the higher energy (by ∼0.1 eV) in ETO-10Nb. The e_g subband, consisting of $d_{x^2-y^2}$ and d_{z^2} states pointing, respectively, to the four side corners and the

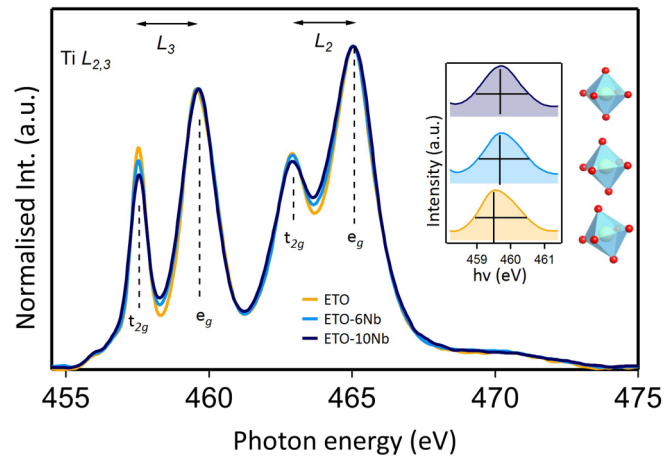

FIG. 3. Ti $L_{3,2}$ XAS spectra obtained from the ETO, ETO-6Nb, and ETO-10Nb. Inset: Ti L_3 e_g edge, showing the change in shape due to Nb incorporation. The spectra are vertically shifted for clarity.

two apex ligand anions of the octahedron, is sensitive to the displacement of Ti atom from the center of the TiO_6 octahedra [23,24]; hence, the shape of the e_g peak can be a measure of the degree of distortion of the octahedron. The asymmetric shape of Ti L_3 e_g in parent ETO compound indicates the off-centered coordination of Ti atom in the TiO_6 octahedron, which is, eventually, a result of the octahedral rotation or tilting. This asymmetric feature of the e_g peak gradually turns symmetric with Nb substitution, indicating the Ti atom tends to restore the centrosymmetric position in ETO-6Nb and ETO-10Nb, similar to that of the earlier reported Ti-based perovskite oxides [25]. The Ti XAS L-edge spectra from ETO and Nb-substituted ETOs thus agree with the earlier speculation on the incorporation of d^1 electrons in Ti t_{2g} states resulting in the decrease in octahedral tilting in Nb-substituted ETOs, which, in turn, affects the hybridization between the Eu $4f$ and Ti $3d$ and O $2p$ resulting in the antiferromagnetic to ferromagnetic phase transition with Nb substitution in ETO [26,27].

C. Hybridization with O 2*p*, XAS at O *K* edge

Taking advantage of the fact that the O K-edge spectra closely resemble the unoccupied p-projected density of states, we assess the delocalized electron states by instigating electron transitions from O $1s$ core level to unoccupied $2p$ states. Figure 4 shows the O K-edge XAS spectra collected from the parent ETO, ETO-6Nb, and ETO-10Nb. The O K-edge XAS spectra of ETO reported here are in good agreement with the O K-edge spectrum observed by an electron-energy-loss spectroscopy study of a polycrystalline ETO [28], matching all the principal transitions. This close matching justifies our analysis of the O K-edge XAS data for the three ETOs given in Fig. 4.

A peak around ∼530.4 eV and a peak around ∼532.4 eV are attributed to the hybridization of O $2p$ with, respectively, t_{2g} and e_g states of B-site cations. Higher-energy peaks at ∼534 and ∼536 eV show predominantly hybridization between Eu $5d$ states with O $2p$, considering the relative positions of the density of states of Eu in ETO [28,29]. The

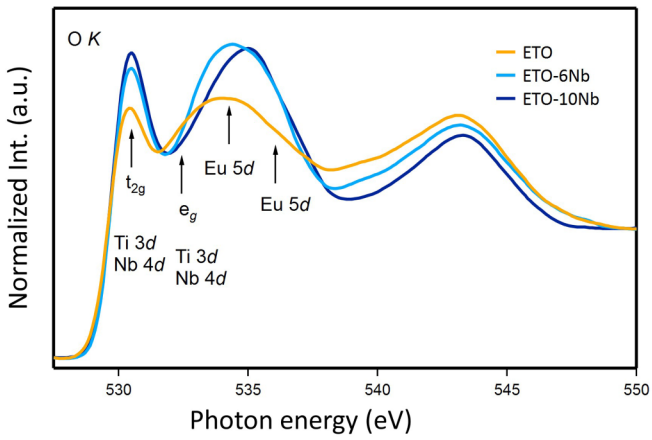

FIG. 4. O *K*-edge XAS spectra collected from ETO, ETO-6Nb, and EBTO-10Nb.

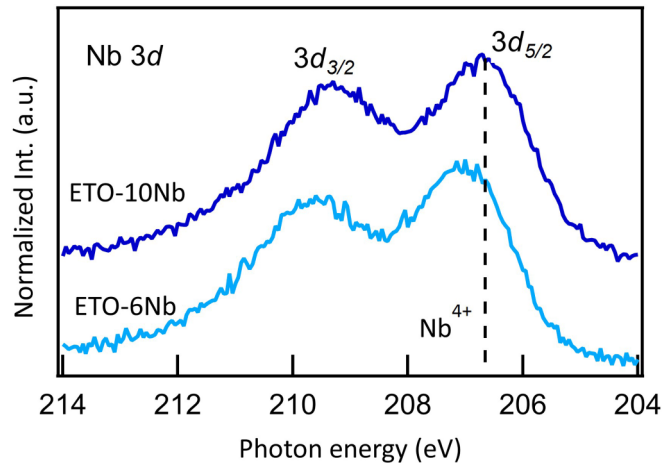

FIG. 5. XPS of Nb 3*d* collected from ETO-6Nb and ETO-10Nb.

modification of O *K*-XAS spectra in ETO-6Nb and ETO-10Nb represents the significant rearrangements of the orbitals and, thus, the hybridizations between the O 2*p* and the cations by the Nb substitution.

Systematic increase in the intensity of the peak at ∼530.4 eV with the Nb substitution implies that the hybridization between the O 2*p* and the t_{2g} states of the B ions comprising Ti and Nb (Ti t_{2g} and Nb t_{2g} overlap in this energy range) is getting stronger. Simultaneously, the peak shifts towards higher energy (0.1 eV for ETO-10Nb); a similar trend is also observed for O *K*-edge XAS spectra in $BaTiO_3$ as an impact of Nb doping at the *B* site [30]. On the other hand, the intensity of the peak at ∼532.4 eV (representing the e_g state) in the Nb-substituted ETOs is lower than that in ETO. This indicates a loss of hybridization between the O 2*p* and the e_g electrons (belonging to both Ti and Nb) relative to the O 2*p*-Ti e_g hybridization in the parent ETO compound. It is also important to note that the intensity of peak at ∼534 is increased for ETO-6Nb in comparison to that in ETO, while the blueshift of the peak (approximately 0.8 eV shift) in ETO-10Nb indicates that the O 2*p* orbitals prefer to hybridize with the t_{2g} and Eu 5*d* states at the cost of O 2*p*-Ti e_g hybridization.

D. XPS of Nb 3*d*

The normalized Nb 3*d* core-level XPS spectra of $EuTi_{1-x}Nb_xO_3$ ($x = 0.06, 0.10$) are shown in Fig. 5. The spectra contain a doublet, situated at about ∼207.1 eV ($3d_{5/2}$) and ∼209.6 eV ($3d_{3/2}$) with a splitting of approximately 2.5 eV indicating a mixture of Nb^{4+} and Nb^{5+} states in ETO-6Nb [31]. The clear shift of the $3d_{5/2}$ state towards lower binding energy by ∼0.4 eV in ETO-10Nb indicates the enhancement Nb^{4+} oxidation states with Nb substitution.

E. Valence-band spectra by UPS

To extract the impact of Nb substitution on the valance band (VB) and, hence, on the Eu 4*f* states, being very close to the Fermi energy level [32], we employ the UPS to ETO and Nb-substituted ETOs. The spectrum [Fig. 6(a)] collected from ETO shows a well-resolved peak around 1.7 eV below the Fermi level, which can be assigned as the Eu 4*f* state (Eu^{2+} ions) [33]. The VB spectra of ETO are qualitatively similar to the earlier reported VB structure of ETO [28–32], including the narrow localized Eu 4*f* state and the broad multistructured O 2*p* states (∼4 to 14 eV from Fermi level) [28].

With Nb substitution, we observe the narrow Eu 4*f* state becomes wider and the valance-band structure is modified just below the Eu 4*f* state, around ∼2–5 eV from the top of the valance band [Figs. 6(b) and 6(c)]. To quantify the change more precisely, we de-convolute the valance-band structures of ETO and Nb-substituted ETOs in the referred energy range (0∼15 eV). The VB of ETO is fitted with Eu 4*f* and four components of O 2*p* which qualitatively agrees with the earlier observation on ETO [28–32]. For Nb-substituted ETOs, an additional peak within 2–4 eV is required to obtain a reasonable fit, without significantly affecting the positions and FWHMs (full width at half maximum) of Eu 4*f* or O 2*p* components, as shown in Figs. 6(b) and 6(c) by the solid blue peak. We attribute this peak to be the lower Hubbard band originated by the freshly generated d^1 electrons due to the Nb substitution at *B* site. The occupied Ti 3*d* states (in valence band) within 2 eV from the Fermi level have been reported in several oxides of Ti [34]. Because the quasilocal plasmons are due to strong electronic correlation effects, i.e., interplay of electron-electron and electron-hole interactions, such plasmonic excitation may not be visible in UPS spectra.

F. Hubbard model and determination of Mott gap (E_g)

Based on the previous studies of ETO [35,36], we can group the *d* states in the conduction band into t_{2g} and e_g states. According to the density-function calculations the lowest unoccupied conduction band (t_{2g}) and the highest occupied valance band (Eu 4*f*) in ETO is separated by a gap reported to be 1 eV [32].

Our XAS study on Ti *L* edge and XPS on Nb 3*d* states reveal that both the Ti and Nb at *B* site have d^1 electronic structures in the Nb-substituted ETOs. Introducing d^1 electrons alters the band structure according to the Hubbard model: The *d* band in Nb-substituted ETOs splits into two subbands by the electron-electron repulsion (*U*) and forms

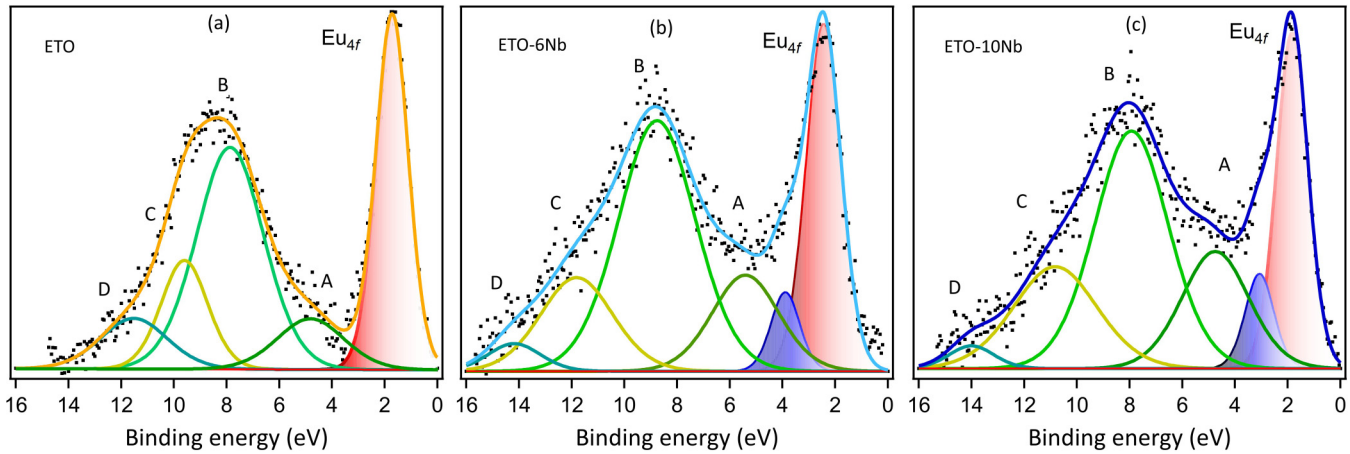

FIG. 6. Comparing valence spectra collected from ETO, ETO-6Nb, and ETO-10Nb. The blue peak within (2–4) eV below Fermi level indicates the LHB formed in ETO-6Nb and ETO-10Nb.

the upper Hubbard band (UHB) and the lower Hubbard band (LHB) separated by the Mott gap E_g (here, $U = E_g + W$; W is the Hubbard bandwidth). We estimate the values of the band gap for the ETO ($E_{g1} = 0.86$ eV), ETO-6Nb ($E_{g2} = 0.96$ eV), and ETO-10Nb ($E_{g3} = 0.54$ eV), shown in Fig. 7, using the optical conductivity (σ_1) defined by

$$\sigma_1(\omega) = \varepsilon_0 \varepsilon_2(\omega)\omega, \tag{5}$$

where ε_0 is the free-space permittivity.

G. The band modulation scheme

Combining the information obtained from the spectroscopy studies, we have drawn the schematic band diagrams of the ETO, ETO-6Nb, and ETO-10Nb in Figs. 8(a)–8(c). In Fig. 8(a), showing the band modulation near Fermi level in ETO, the band gap between Eu $4f$ and Ti $3d$ is 0.86 eV and the CT energy, i.e., transition between O $2p$ and Ti $3d$ (t_{2g}), is 5 eV. We notice that our estimated CT energy in ETO is lower than that calculated by Akamatsu *et al.* [32] Our UPS data, on the other hand, show a reasonable match with

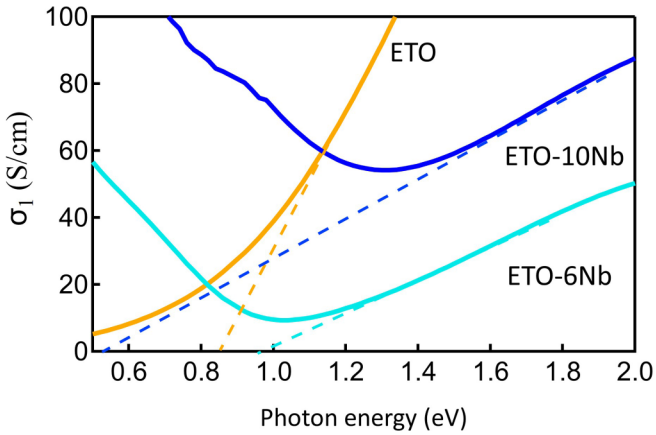

FIG. 7. Estimation of band-gap energy (E_g) from the optical conductivity (σ_1) data. E_g for ETO (0.86 eV), ETO-6Nb (0.96 eV), and ETO-10Nb (0.54 eV) are estimated by extrapolating the optical conductivity (σ_1) onto the energy axis shown by the dashed lines.

the valance-band structure reported in the same work. We, therefore, retain the relative energy positions of the valance band (this includes Eu $4f$ and the O $2p$ states) in ETO as described by Akamatsu *et al.* [32], while the Ti t_{2g} band in Fig. 4(a) is placed at 0.86 eV above the Eu $4f$ state. Ti t_{2g} and e_g states are 2 eV apart as we have estimated from Ti L-edge XAS (Fig. 3), which also helps to determine the widths (taken approximately as the FWHM of Ti t_{2g} and e_g states in Fig. 3 of these two states to be 0.7 and 1.5 eV, respectively.

In Fig. 8(b), the band structure of ETO-6Nb is modified with the Nb substitution: the Hubbard bands are formed and are separated by the E_{g_2} estimated as 0.96 eV, whereas, the *charge-transfer* energy between O $2p$ and UHB is ∼5.2 eV. Our UPS results show that the narrow localized Eu $4f$ state is still cosharing the top position of the valance band with LHB. Mixing of Eu $4f$ and d orbitals has previously been predicted for ETO [26–32]. With further Nb substitution in ETO-10Nb [see Fig. 8(c)], the position of Eu $4f$ does not change (supporting the valance-band spectra), but the gap between LHB and UHB becomes narrower ($E_{g3} \sim 0.54$ eV) as a combined effect of increase in U (due to the larger number of Nb $4d^1$ electrons) and even a greater increase in W (contributed by the wider $4d$ orbital of Nb) following the relation $U = W + E_g$.

H. The quasilocal electrons in ETO/EBTOs

We can now combine our understanding of the Nb-substituted ETO in the light of the previous study on Nb-substituted EBTOs [8] to identify the origin of the unconventional plasmons in ETO-10Nb. In ETO and EBTO, we find that the d^1 (both Nb $4d^1$ and Ti $3d^1$) electrons are originated by the Nb substitution within the many-body interactions of intermixing of f-d states: notably, a diluted f-d hybridization exists in both perovskites. As we showed in previous study with EBTO [8], these partially free d^1 electrons make a direct contribution in the formation of the plasmonic excitation. The plasmonic oscillation, associated with these correlated electrons, therefore takes a quasilocal character. We argue that the formation of quasilocal plasmon in ETO-10Nb also has a similar origin as those of Nb-substituted EBTOs, i.e., the

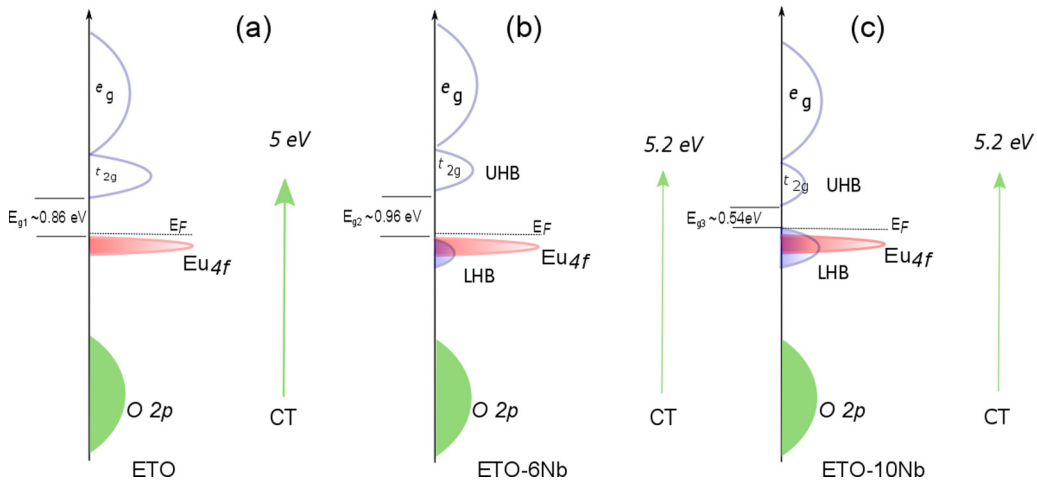

FIG. 8. Possible band-structure scheme. (a) ETO, (b) ETO-6Nb, and (c) ETO-10Nb. Hubbard interaction $U \sim E_g + W$. E_{g_1}, E_{g_2}, and E_{g_3} are the band gaps (in eV) for ETO, ETO-6Nb, and ETO-10Nb, respectively; W is Hubbard-band width. E_F denotes Fermi level; CT is *change transfer*.

d^1 electrons in the Nb-substituted ETOs. The low plasmon energy (in the IR range) reflects the low participation and/or high correlation of the d^1 electrons. The degree of the quasilocality is significantly affected by the *f-d* hybridization and, thus, by the Eu $4f$ electrons. The boundness of the quasilocal electrons in the strongly correlated systems (example: Nb-substituted ETO/EBTOs) can be quantified by the density (n) and the effective mass (m^*) of the electrons participating in the plasmonic excitation.

According to the free-electron model, the plasmonic energy E_p is related to n and m^* by the relation $E_p^2 = \hbar^2[\frac{ne^2}{m^*\varepsilon_0}]$, where e is the elementary charge of electron and ε_0 is the permittivity of the free space. The above relation is valid for the free electrons (i.e., Drude model) and can be used as a good first approximation for the strongly correlated electron systems (example: ETO/EBTOs), where the main difference comes from the ratio n/m^* as, in the free-electron model, the participating electrons are treated as *free* and, therefore, have effective mass $m^* = m$; m is the rest mass of electron. In strongly correlated electron systems, on the other hand, the participating electrons are correlated. By using the free-electron model we then consider the electrons to be free (i.e., we impose the $m^* = m$ condition) and modify n for the strongly correlated electrons. The modified n, termed as the *effective* free-electron density n', now satisfies $n/m^* = n'/m$. This approach simplifies the complexity of the strongly correlated electrons allowing us to express the vibrations (in this case plasmonic excitation) of electrons in terms of the effective free-electron density n'. Our study with ETOs and EBTOs have revealed that the correlation between the electronic states for the d^1 electrons are influenced by the *f-d* and *p-d* hybridizations affecting the effective mass distribution among the quasilocal electrons yielding different n' and, thus, different E_p.

To elaborate the above concept, we compare the n' for ETO-10Nb with those in Nb-substituted EBTOs [8]. Our estimation suggested nearly 30% of the d^1 electrons, acting as free electrons, contribute in the quasilocal plasmon excitations in EBTOs. This means the entire d^1 population in Nb-substituted EBTOs is only 30% free (i.e., $n' = 0.3$) or, in other words, has an average effective mass nearly three times of the rest mass of electron (i.e., $m^* \sim 3\,m$). On the similar line of discussion, the plasmon energy 0.54 eV in ETO-10Nb (for $x = 0.1$) estimates $n' \sim 14\%$ of the d^1 population giving $m^* \sim 7\,m$. We note that while Nb-substituted EBTOs show the effective electron masses close to that of $SrVO_3$, the ETO-10Nb shows even a higher m^* that is close to those of a series of strongly-correlated oxides $Nd_{2-x}Ce_xCuO_4$ ($x = 0-1.5$) studied as prospective transparent conductors [37].

In the above section, we discuss the importance of the strength of the correlations among electronic states determining the energy of the plasmonic excitations in the IR range. By controlling the correlations (or hybridizations) we achieve a plasmonic energy of 0.54 eV in ETO-10Nb, which is lower than the 0.86 eV for the EBTO-10Nb at room temperature. The unconventional plasmon energy in ETO-10Nb is much lower than the energy of, for example, surface plasmons of Au and Ag [38]. The critical advantage of the unconventional plasmons that has been reported in Nb-substituted bulk ETO, Nb-substituted bulk EBTOs, and thin films of $Sr_{(1-x)}Nb_{(1-y)}O_{3+\delta}$ perovskites family lies in their low-loss character. In Fig. 9, we show the comparison of the plasmon energies and the intensities of the associated loss functions for these unconventional plasmons.

Apart from the above-mentioned similarities in the origin and the properties of the unconventional plasmonic excitations, there are some critical differences in the formation of these plasmons in Nb-substituted ETO and EBTOs. The XAS study at Ti $L_{3,2}$ and O K edges shows the decrease in tilting angle of the TiO_6 octahedron due to Nb substitution [26,27] is caused by the significant modified hybridization between O $2p$ and Ti $3d$ states as well as the hybridization between Eu $4f$ and Ti $3d$ states [20]. The strain developed in the bulk ETO structure by a rotated TiO_6 octahedron is decreased at room temperature by the Nb substitution, which has been reported by the earlier experiments to trigger a conversion of

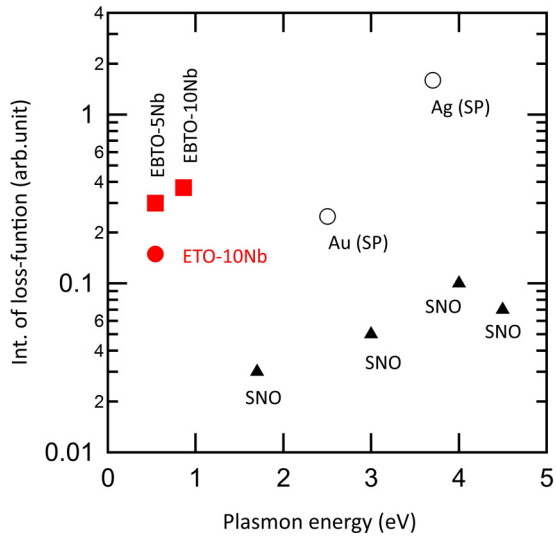

FIG. 9. Comparison of the unconventional plasmon energy and intensity of the associated loss functions in Nb-substituted $EuTiO_3$ (ETO-10Nb), Nb-substituted $Eu_{0.30}Ba_{0.70}TiO_3$ (EBTO-5Nb and EBTO-10Nb) [8], and thin films of $Sr_{(1-x)}Nb_{(1-y)}O_{3+\delta}$ (SNO) [7]. Surface plasmons (SP) and their loss functions for Au and Ag thin films [38] are also included for reference.

antiferromagnetic state (ETO) to ferromagnetic states (Nb-substituted ETOs) [27]. In EBTO, however, the electron-lattice coupling appears to be nearly unaffected by the Nb substitution. By viewing EBTO as a derived composition of ETO by sharing the *A* site with Eu and Ba, it appears that by adding Ba at the *A* site we may allow the octahedron to relax.

The d^1 electrons generated due to the Nb substitution in ETO also alter the conductivity of the system [39]. However, as our present comprehensive study reveals that the electronic structure of the Nb substituted ETO system is not that of a conventional $ATiO_3$ group (A = non-Eu cation), the electron transport mechanism is expected to be significantly different due to primarily the Eu $4f$ bands as also observed in Nb-substituted $Eu_{0.70}Ba_{0.30}TiO_3$ [8]. In EBTO, which is a Mott insulator, the Nb substitution widens the Mott gap with the formation of midgap states that triggers the IMT transition in Nb-substituted EBTO. In Nb-substituted ETO, the Nb substitution transforms the intrinsic insulator/semiconductor ETO into a Mott insulator which narrows the Mott gap with the amount of Nb substitution.

IV. CONCLUSIONS

In summary, we present an unconventional plasmon formation within the IR range (<1 eV) at room temperature of Nb-substituted ETOs. The plasmons are of low loss in character and generated by many-body interactions, the interplay of quasilocal d^1 electrons, TiO_6 octahedral tilting, and hybridizations of Eu $4f$-Ti $3d$ and O $2p$-Ti $3d$, which are highly controllable with Nb concentration. Our result opens an opportunity to explore plasmons in multiferroics doped perovskite oxides.

ACKNOWLEDGMENTS

This work is supported by the Ministry of Education Tier 2 (Grants No. MOE2015-T2-2-065, No. MOE2017-T2-1-135, No. MOE2015-T2-2-147, and No. MOE2016-T2-1-054), Singapore National Research Foundation under its Competitive Research Funding (Grants No. NRF-CRP 8-2011-06 and No. NRF-CRP15-2015-01) and Ministry of Education Tier 1 (Grants No. R-144-000-398-114, No. R-144-000-373-112, No. R-144-000-349-112, and No. R-144-000-423-114), 2015 PHC Merlion project, and NUS Core Support No. C-380-003-003-001. The authors would like to acknowledge the Singapore Synchrotron Light Source for providing the facility necessary for conducting the research. The SSLS is a National Research Infrastructure under the National Research Foundation Singapore.

[1] G. V. Naik, J. Kim, and A. Boltasseva, Opt. Mater. Express **1**, 1090 (2011).
[2] P. Q. Liu, I. J. Luxmoore, S. A. Mikhailov, N. A. Savostianova, F. Valmorra, J. Faist, and G. R. Nash, Nat. Commun **6**, 8969 (2015).
[3] Y. Zhong, S. D. Malagari, T. Hamilton, and D. M. Wasserman, J. Nanophotonics **9**, 093791 (2015).
[4] A. Sobhani, M. W. Knight, Y. Wang, B. Zheng, N. S. King, L. V. Brown, Z. Fang, P. Nordlander, and N. J. Halas, Nat. Commun **4**, 1643 (2013).
[5] G. V. Naik, V. M. Shalaev, and A. Boltasseva, Adv. Mater. **25**, 3264 (2013).
[6] E. G. C. P. van Loon, H. Hafermann, A. I. Lichtenstein, A. N. Rubtsov, and M. I. Katsnelson, Phys. Rev. Lett. **113**, 246407 (2014).
[7] T. C. Asmara, D. Wan, Y. Zhao, M. A. Majidi, C. T. Nelson, M. C. Scott, Y. Cai, B. Yan, D. Schmidt, M. Yang, T. Zhu, P. E. Trevisanutto, M. R. Motapothula, Y. P. Feng, M. B. H. Breese, M. Sherburne, M. Asta, A. Minor, T. Venkatesan, and A. Rusydi, Nat. Commun. **8**, 15271 (2017).
[8] A. Chaudhuri, K. Rubi, T. C. Asmara, X. Chi, X. J. Yu, R. Mahendiran, and A. Rusydi, Phys. Rev. B **98**, 165303 (2018).
[9] X. Yin, M. A. Majidi, X. Chi, P. Ren, L. You, N. Palina, X. Yu, C. Diao, D. Schmidt, B. Wang, P. Yang, M. B. H. Breese, J. Wang, and A. Rusydi, NPG Asia Mater **7**, e196 (2015).
[10] T. C. Asmara, I. Santoso, and A. Rusydi, Rev. Sci. Instrum. **85**, 123116 (2014).
[11] X. J. Yu, C. Z. Diao, T. Venkatesan, M. B. H. Breese, and A. Rusydi, Rev. Sci. Instrum. **89**, 113113 (2018).
[12] X. Yu, O. Wilhelmi, H. O. Moser, S. V. Vidyaraj, X. Gao, A. T. S. Wee, T. Nyunt, H. Qian, and H. Zheng, J. Electron. Spectrosc. Relat. Phenom. **144**, 1031 (2005).
[13] S. Zollner, A. A. Demkov, R. Liu, P. L. Fejes, R. B. Gregory, P. Alluri, J. A. Curless, Z. Yu, J. Ramdani, R. Droopad, T. E. Tiwald, J. N. Hilfiker, and J. A. Woollam,

J. Vac. Sci. Technol., B: Microelectron. Nanometer Struct.–Process., Meas., Phenom. **18**, 2242 (2000).
[14] L. Sponza, V. Véniard, F. Sottile, C. Giorgetti, and L. Reining, Phys. Rev. B **87**, 235102 (2013).
[15] J. H. Lee, X. Ke, N. J. Podraza, L. F. Kourkoutis, T. Heeg, M. Roeckerath, J. W. Freeland, C. J. Fennie, J. Schubert, D. A. Muller, P. Schiffer, and D. G. Schlom, Appl. Phys. Lett. **94**, 212509 (2009).
[16] H. Akamatsu, K. Fujita, H. Hayashi, T. Kawamoto, Y. Kumagai, Y. Zong, K. Iwata, F. Oba, I. Tanaka, and K. Tanaka, lnorg. Chem. **51**, 4560 (2012).
[17] V. Goian, S. Kamba, O. Pacherová, J. Drahokoupil, L. Palatinus, M. Dušek, J. Rohlíček, M. Savinov, F. Laufek, W. Schranz, A. Fuith, M. Kachlík, K. Maca, A. Shkabko, L. Sagarna, A. Weidenkaff, and A. A. Belik, Phys. Rev. B **86**, 054112 (2012).
[18] K. Z. Rushchanskii, N. A. Spaldin, and M. Ležaić, Phys. Rev. B **85**, 104109 (2012).
[19] Y. Yang, W. Ren, D. Wang, and L. Bellaiche, Phys. Rev. Lett. **109**, 267602 (2012).
[20] H. Akamatsu, Y. Kumagai, F. Oba, K. Fujita, K. Tanaka, and I. Tanaka, Adv. Funct. Mater. **23**, 1864 (2013).
[21] F. M. F. de Groot, M. O. Figueiredo, M. J. Basto, M. Abbate, H. Petersen, and J. C. Fuggle, Phys. Chem. Miner. **19**, 140 (1992).
[22] C. Chen, J. Avila, E. Frantzeskakis, A. Levy, and M. C. Asensio, Nat. Commun. **6**, 8585 (2015).
[23] J. C. Jan, K. P. Krishna Kumar, J. W. Chiou, H. M. Tsai, H. L. Shih, H. C. Hsueh, S. C. Ray, K. Asokan, W. F. Pong, M. H. Tsai, S. Y. Kuo, and W. F. Hsieh, Appl. Phys. Lett. **83**, 3311 (2003).
[24] P. Nachimuthu, S. Thevuthasan, E. M. Adams, W. J. Weber, B. D. Begg, B. S. Mun, D. K. Shuh, D. W. Lindle, E. M. Gullikson, and R. C. C. Perera, J. Phys. Chem. B **109**, 1337 (2005).
[25] H. Zhao, J. Miao, L. Zhang, Y. Rong, J. Chen, J. Deng, R. Yu, J. Cao, H. Wang, and X. Xing, Dalton Trans. **45**, 1554 (2016).
[26] T. Birol and C. J. Fennie, Phys. Rev. B **88**, 094103 (2013).
[27] L. Li, J. R. Morris, M. R. Koehler, Z. Dun, H. Zhou, J. Yan, D. Mandrus, and V. Keppens, Phys. Rev. B **92**, 024109 (2015).
[28] T. Kolodiazhnyi, M. Valant, J. R. Williams, M. Bugnet, G. A. Botton, N. Ohashi, and Y. Sakka, J. Appl. Phys. **112**, 083719 (2012).
[29] R. Rajeev, N. Hasan Sadat, and P. Rossitza, J. Phys.: Condens. Matter **19**, 406217 (2007).
[30] Y. Shao, C. Maunders, D. Rossouw, T. Kolodiazhnyi, and G. A. Botton, Ultramicroscopy **110**, 1014 (2010).
[31] K. Isawa, R. Itti, J. Sugiyama, N. Koshizuka, and H. Yamauchi, Phys. Rev. B **49**, 3534 (1994).
[32] H. Akamatsu, Y. Kumagai, F. Oba, K. Fujita, H. Murakami, K. Tanaka, and I. Tanaka, Phys. Rev. B **83**, 214421 (2011).
[33] R. Vercaemst, D. Poelman, R. L. Van Meirhaeghe, L. Fiermans, W. H. Laflère, and F. Cardon, J. Lumin. **63**, 19 (1995).
[34] M. T. Greiner and Z.-H. Lu, NPG Asia Mater. **5**, e55 (2013).
[35] J. Zaanen, G. A. Sawatzky, and J. W. Allen, Phys. Rev. Lett. **55**, 418 (1985).
[36] M. Mizumaki, A. Agui, K. Yoshii, and M. Nakazawa, Solid State Ionics **172**, 565 (2004).
[37] L. Zhang, Y. Zhou, L. Guo, W. Zhao, A. Barnes, H.-T. Zhang, C. Eaton, Y. Zheng, M. Brahlek, H. F. Haneef, N. J. Podraza, M. H. W. Chan, V. Gopalan, K. M. Rabe, and R. Engel-Herbert, Nat. Mater. **15**, 204 (2015).
[38] A. Pulisciano, S. J. Park, and R. E. Palmer, Appl. Phys. Lett. **93**, 213109 (2008).
[39] K. Yoshiro, M. Hideo, F. Koji, K. Itsuhiro, S. Minoru, M. Shunsuke, and T. Katsuhisa, Jpn. J. Appl. Phys. **53**, 05FJ07 (2014).